

Line-edge roughness transfer function and its application to determining mask effects in EUV resist characterization

Patrick P. Naulleau and Gregg M. Gallatin

The control of line-edge roughness (LER) of features printed in photoresist poses significant challenges to next-generation lithography techniques such as extreme-ultraviolet (EUV) lithography. Achieving adequately low LER levels will require accurate resist characterization as well as the ability to separate resist effects from other potential contributors to LER. One significant potential contributor is LER on the mask. Here we explicitly study the mask to resist LER coupling using both analytical and computer-simulation methods. We present what is to our knowledge a new imaging transfer function referred to as the LER transfer function (LTF), which fundamentally differs from both the conventional modulation transfer function and the optical transfer function. Moreover, we present experimental results demonstrating the impact of current EUV masks on projection-lithography-based LER experiments. © 2003 Optical Society of America

OCIS codes: 110.4100, 110.4850, 110.4980, 110.3960.

1. Introduction

As the microelectronics industry pushes to smaller and smaller feature sizes, the issue of edge roughness of features printed in photoresist, commonly referred to as line-edge roughness or LER, becomes increasingly important. This poses significant challenges to next-generation lithography techniques such as extreme-ultraviolet (EUV) lithography,^{1–3} which could enter production at the 45-nm node. At this node, the International Technology Roadmap for Semiconductors⁴ calls for a resist contribution to LER of less than 2 nm.

It is evident that achieving these low LER levels will require accurate resist characterization as well as the ability to separate resist effects from other potential contributors to LER. Much effort has been directed to characterizing EUV resists,^{5–8} with the most straightforward being actual projection lithog-

raphy tests by use of advanced prototype EUV lithography tools.^{8–10} When using such tools to characterize LER, however, the control and understanding of system-level effects on LER is crucial. One such potential system-level effect is LER on the mask used in the lithography step.

Roughness on the mask will, to some extent, transfer to roughness in the printed feature. In this paper, we explicitly study this coupling using both analytical and computer-simulation methods. We present what is to our knowledge a new imaging transfer function referred to as the LER transfer function (LTF), which, as shown here, fundamentally differs from both the conventional optical transfer function (OTF) and the modulation transfer function (MTF).¹¹ Moreover, we present experimental results demonstrating the impact of current EUV masks on projection-lithography-based LER experiments.

2. Derivation of the Line-Edge Roughness Transfer Function

We begin by deriving the transfer function for mask line-edge roughness to resist line-edge roughness in the context of a scalar image model in the thin mask approximation and in assuming a threshold model for the resist. The scalar approximation for image formation is sufficient at a low numerical aperture (NA) such as those typically used in EUV optics. We note,

P. P. Naulleau is with the Center for X-Ray Optics, Lawrence Berkeley National Laboratory, 1 Cyclotron Rd., Berkeley, California 94720. G. M. Gallatin is with IBM Semiconductor Research and Development Center, Research Division, T. J. Watson Research Center, Yorktown Heights, New York 10598.

Received 27 January 2003; revised manuscript received 4 March 2003.

0003-6935/03/173390-08\$15.00/0

© 2003 Optical Society of America

however, that the analysis presented here could be refined by removing the thin mask approximation, which strictly speaking is of limited accuracy for EUV masks.

Within the scalar approximation the image intensity is given by

$$I(\mathbf{x}) = \int d^2x_1 d^2x_2 P(\mathbf{x} - \mathbf{x}_1) P^*(\mathbf{x} - \mathbf{x}_2) O(\mathbf{x}_1) O^*(\mathbf{x}_2) C(\mathbf{x}_1, \mathbf{x}_2). \quad (1)$$

Here P is the amplitude point-spread function of the optics given by

$$P(\mathbf{x}) = \int d^2\beta \theta[(NAk)^2 - \beta^2] \exp[i\beta \cdot \mathbf{x} + iw(\beta)], \quad (2)$$

O is the object or mask transmission pattern, which, for a binary mask, is simply a 0 or 1 as a function of position $\mathbf{x} = (x, y)$ in the mask plane, and C is the autocorrelation of the illumination, i.e., the partial coherence. The parameter $k = 2\pi/\lambda$ with λ the wavelength in a vacuum, NA is the numerical aperture of the projection optics, and $w(\beta)$ is the aberrated wavefront in radians. For simplicity we will set $w(\beta)$ to zero and so that the result derived below applies to diffraction limited, in-focus, optics. Finally, the function $\theta(X)$ is a Heaviside step defined as

$$\theta(X) = \begin{cases} 1 & \text{for } X > 0 \\ 0 & \text{for } X < 0 \end{cases}. \quad (3)$$

In Eq. (2), $\theta[(NAk)^2 - \beta^2]$ represents the circular pupil of the optical system in pupil plane coordinates $\beta = (\beta_x, \beta_y)$.

For Köhler illumination with tophat fill σ , the function C is given by

$$C(\mathbf{x}_1, \mathbf{x}_2) = \int d^2s \theta[(\sigma NAk)^2 - \beta^2] \times \exp[i\mathbf{s} \cdot (\mathbf{x}_1 - \mathbf{x}_2)], \quad (4)$$

where σ represents the ratio of the illumination angular extent to the imaging optic entrance NA . Substituting Eqs. (2) and (4) into (1) yields

$$I(\mathbf{x}) = \int d^2s \theta[(\sigma NAk)^2 - \beta^2] \times \left| \int d^2\beta \exp(i\beta \cdot \mathbf{x}) \theta[(NAk)^2 - \beta^2] \tilde{O}(\beta - \mathbf{s}) \right|^2, \quad (5)$$

where $\tilde{O}(\beta)$ is the Fourier transform of the object function

$$\tilde{O}(\beta) = \int d^2x \exp(-i\beta \cdot \mathbf{x}) O(\mathbf{x}). \quad (6)$$

Assuming a threshold resist model the resist line-edge position is given implicitly by the values of \mathbf{x} that satisfy

$$I(\mathbf{x}) = T = \text{threshold value}. \quad (7)$$

It follows from the above relation that a small variation in intensity, δI , induces a variation in the resist-edge position given by

$$\delta x = \frac{\delta I(\mathbf{x}) \nabla I(\mathbf{x})}{|\nabla I(\mathbf{x})|^2} \bigg|_{\mathbf{x}=\mathbf{x}_{\text{edge}}}. \quad (8)$$

For a single edge oriented along the x axis at $y = 0$ we have explicitly

$$\delta y(x) = \frac{\delta I(x, y)}{\partial_y I(x, y)} \bigg|_{y=0} = \left(\frac{\delta I(x, 0)}{I(x, 0)} \right) \left(\frac{I(x, y)}{\partial_y I(x, y)} \right) \bigg|_{y=0}. \quad (9a)$$

Thus the transfer function for mask-edge roughness to resist-edge roughness is given simply by the fractional variation in the image intensity $\delta I/I$ times the reciprocal of the image log slope $\nabla \ln(I)$, both evaluated at the nominal edge position. To avoid line-end effects we assume an infinitely long edge, in which case $I(x, 0)$ and $[\partial_y I(x, y)]_{y=0}$ are both independent of x and the entire x dependence of the edge position $\delta y(x)$ comes from the x dependence of $\delta I(x, 0)$. Using $I(x, 0) = T$ and using the notation ILS for the image log slope evaluated at the nominal edge position, we can rewrite Eq. (9a) as

$$\delta y(x) = \frac{\delta I(x, 0)}{T \text{ILS}} \quad (9b)$$

The object function for the type of edge we are considering is given by $\theta[y - h(x)]$ where $h(x)$ is the deviation in the position of the mask edge from the ideal edge $\theta(y)$, i.e., $h(x)$ is the mask-edge roughness.

Fourier transforming the rough edge $\theta[y - h(x)]$ and keeping terms only up to the first order in h , which is valid for the expected small roughness yields

$$\tilde{O}(\beta) = -\frac{2\pi i}{\beta_y - i\epsilon} \delta(\beta_x) - 2\pi \tilde{h}(\beta), \quad (10)$$

where

$$\tilde{h}(\beta) = \int dx \exp(-i\beta_x x) h(x) \quad (11)$$

and ϵ is an infinitesimal positive real number that is to be set to zero at the end of the calculation. Its function is simply bookkeeping: it specifies how to circulate the $1/\beta_y$ pole in the complex plane when

performing the β_y integration. The standard representation of this function is

$$\frac{1}{\beta_y - i\epsilon} = i\pi\delta(\beta_y) + \text{PP}\left(\frac{1}{\beta_y}\right), \quad (12)$$

where PP stands for principal part. Note that the first term is imaginary and the PP term is real.

In Eq. (10) the first term is the Fourier transform of the ideal edge, $\theta(y)$, whereas the second term is the first-order correction due to the mask-edge roughness, $h(x)$. We will keep terms only up to the first order in h throughout the analysis. This, by definition, yields a linear roughness transfer function. The higher-order terms correspond to nonlinear transfer functions.

Combining the above results for $y = 0$ yields

$$\begin{aligned} \int d^2\beta \exp(i\beta_x x) \theta[(NAk)^2 - \beta^2] \tilde{O}(\beta - s) &= \exp(is_x x) \\ &\times \left[2\pi^2 - 2\pi i \ln \left(\frac{\sqrt{(NAk)^2 - s_x^2} - s_y}{\sqrt{(NAk)^2 - s_x^2} + s_y} \right) \right. \\ &- 4\pi \int_{-NAk}^{+NAk} d\beta_x \exp(i\beta_x x) \tilde{h}(\beta_x \\ &- s_x) \sqrt{(NAk)^2 - \beta_x^2} \left. \right]. \end{aligned} \quad (13)$$

Taking the absolute value squared of the above result and by use of $\tilde{h}(\beta_x) = \tilde{h}^*(-\beta_x)$ that follows from $h(x) = h^*(x)$, the ln terms cancel and finally, dropping the unnecessary x subscripts, we have, to the first order in h ,

$$\begin{aligned} \delta y(x) &= \frac{1}{\text{TILS}} \int d\beta \exp(i\beta x) \tilde{h}(\beta) \\ &\times \left(-32\pi^3 \int ds \left\{ \theta[(\sigma NAk)^2 - s^2] \right. \right. \\ &\times \theta[(NAk)^2 - (\beta + s)^2] \\ &\times \left. \left. \sqrt{(\sigma NAk)^2 - s^2} \sqrt{(NAk)^2 - (\beta + s)^2} \right\} \right) \\ &= \frac{N}{\text{TILS}} \int d\beta \exp(i\beta x) \tilde{h}(\beta) \text{LTF}(\beta). \end{aligned} \quad (14)$$

Here N is a normalization factor defined by the term in parentheses evaluated at $\beta = 0$ so that the transfer function satisfies $\text{LTF}(\beta = 0) = 1$. Note that the θ functions in the integrand appropriately limit the range of the s integration for any value of β so that each square root factor, and hence LTF, is always real. Thus we can simplify the integrand by writing

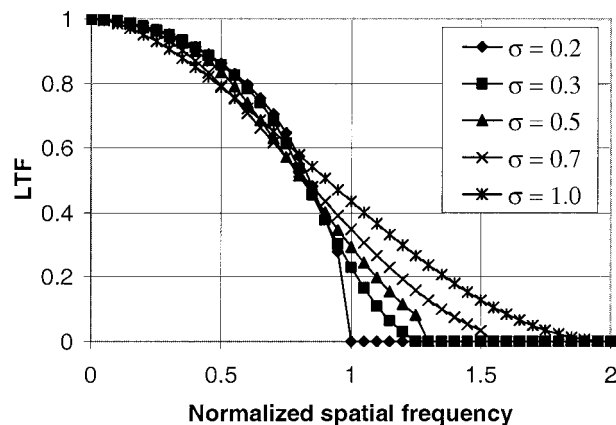


Fig. 1. LTF for various σ values as a function of the normalized spatial frequency (normalized to the coherent cutoff frequency).

it as the product of the real part of each square root factor so that

$$\text{LTF}(\bar{\beta}) = \frac{\int d\bar{s} \text{Re}(\sqrt{\sigma^2 - \bar{s}^2}) \text{Re}(\sqrt{1 - (\bar{s} - \bar{\beta})^2})}{\int d\bar{s} \text{Re}(\sqrt{\sigma^2 - \bar{s}^2}) \text{Re}(\sqrt{1 - \bar{s}^2})}, \quad (15)$$

where $\bar{s} = s/NAk$ and $\bar{\beta} = \beta/NAk$, i.e., \bar{s} and $\bar{\beta}$ are specified as fractions of the pupil radius NAk . It is worth noting that $\text{LTF}(\beta)$ as defined above is neither the standard OTF nor the standard MTF of the optics and hence constitutes a new transfer function. The form of Eq. (14) indicates that $\text{LTF}(\beta)$ functions as a filter: the Fourier transform of the mask contribution to resist LER is given by $\text{LTF}(\beta)\tilde{h}(\beta)$. In terms of the power spectrum of the mask contribution to resist LER it is given by $|\text{LTF}(\beta)|^2|\tilde{h}(\beta)|^2$.

Figure 1 shows the LTF for various σ values as a function of normalized spatial frequency (normalized to the coherent cutoff frequency, i.e., the pupil radius NAk). As is the case for the conventional OTF, smaller σ values tend to lead to stronger modulation at normalized frequencies below 1 and weaker modulation at normalized frequencies of greater than 1. The LTF, however, has a sharper cutoff than the conventional OTF. This is most readily noted by considering the highest coherent condition in plotted Fig. 1 ($\sigma = 0.2$), where the LTF is characterized by a significant and gradual roll-off at normalized frequencies below 1. We note that the conventional OTF would simply be unity at normalized frequencies below 0.8 and quickly go to zero at normalized frequencies greater than 1.

3. Simulation-Based Determination of the LTF

It is also instructive to investigate the LTF from the computer-modeling point of view. In this case, computer-based aerial-image modeling is used to calculate the aerial-image LER response as a function of input LER frequency. In addition to providing phys-

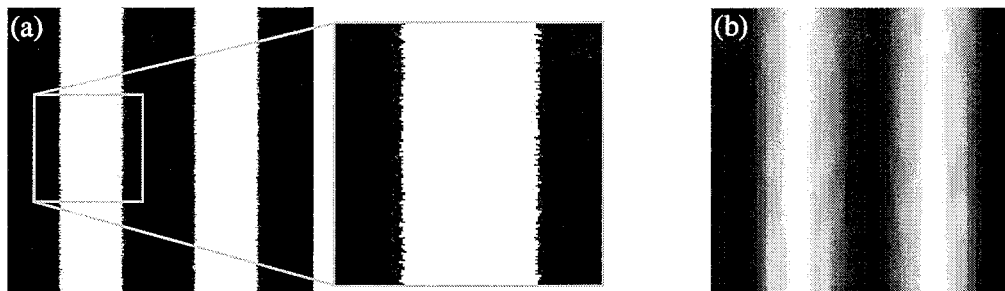


Fig. 2. (a) LTF simulation input mask with a white LER spectrum and 100-nm features, (b) computer-calculated aerial assuming the 0.1-NA engineering test stand Set-2 optic including the EUV-measured wavefront aberrations and assuming partially coherent illumination ($\sigma = 0.7$).

ical insight into the LTF, this method also facilitates the incorporation of parameters, such as aberrations in the optical system and unconventional illumination conditions.

One method for computer-based modeling of the LTF involves generating a mask pattern containing a white LER spectrum [Fig. 2(a)] and calculating the LER spectrum from the resulting aerial image [Fig. 2(b)]. Figure 3 shows the resulting input and output LER power spectral densities (PSDs). In this case, the 0.1-NA EUV engineering test stand Set-2 optic^{12,13} is modeled. The aerial-image modeling includes the measured wavefront aberrations from the optic¹⁴ and assumes partially coherent disk illumination with a coherence factor (σ) of 0.7. The mask is modeled as a simple thin binary mask.

The PSDs shown in Fig. 3 are actually averages from four separate simulations with four statistically independent white-noise LER masks. This averaging is performed to avoid holes in the characterization frequencies, which occur when a single white-noise mask is used. The noise floor observed in the PSD is due to the pixelation limits in the various simulation and processing steps. We define the LTF as the

square root of the aerial-image PSD divided by the white-noise mask PSD (Fig. 4). It is evident that in the limit of infinite averaging, the white-noise mask PSD will by definition be uniform and that the aerial-image PSD will be equal to the white-noise mask PSD at the spatial frequency of 0. Thus the LTF can be taken simply as the square root of normalized aerial-image LER PSD in the infinite averaging limit.

Next we consider the alternate calculation approach of using a series of mask patterns, each with a unique LER frequency and determining the LER from the resulting aerial images. This provides a discrete sampling of the LTF. Figure 5 illustrates this method. Figure 5(a) shows an example sinusoidal LER mask with an LER period of 210 nm and a feature CD of 100 nm, and Fig. 5(b) shows the calculated aerial image. This serves as a single-frequency probe of the LTF. By generating a variety of these single-frequency probes, the LTF can be built up as shown in Fig. 5(c). The linearity of this process was verified by considering a single spatial frequency at three different amplitudes covering an order of magnitude. As required for linearity, the ratio of the output LER magnitude to the input LER

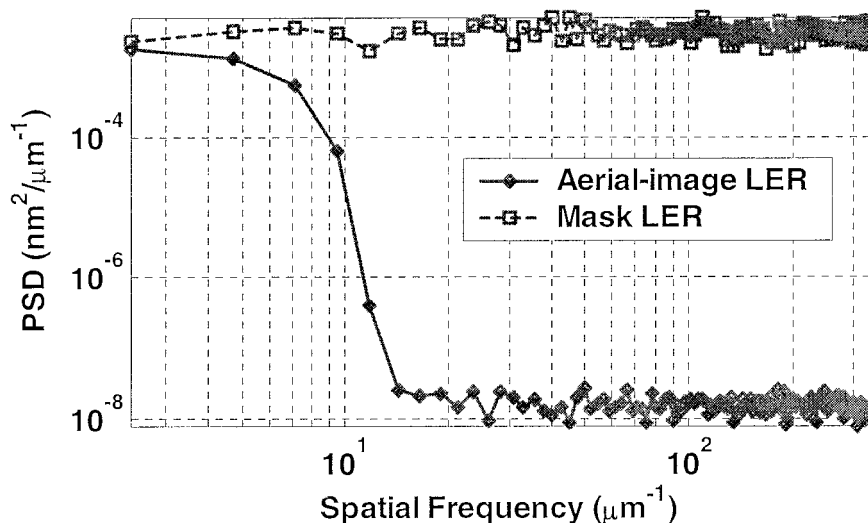


Fig. 3. LER PSDs for the input mask (upper trace) and output aerial image (lower trace). Average of calculations from four independent realizations of the process described in Fig. 2.

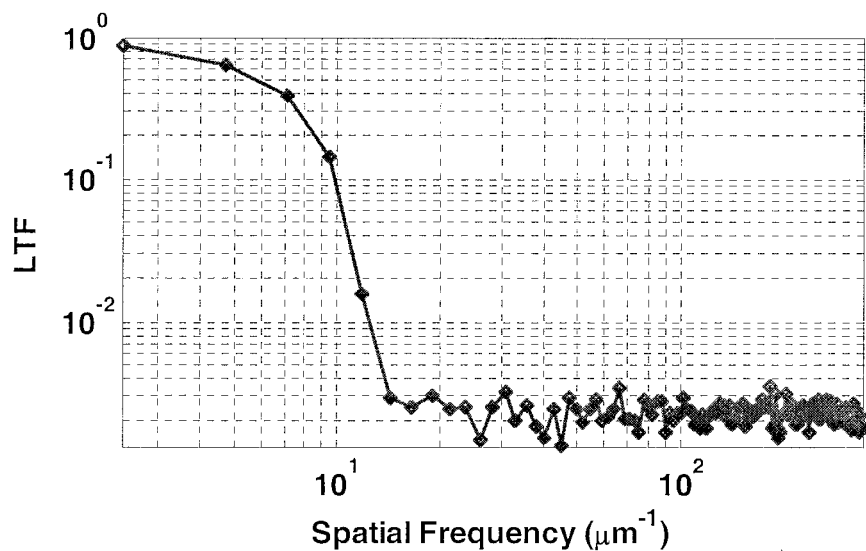


Fig. 4. LTF derived by taking the square root of the aerial-image LER PSD divided by the white-noise mask PSD from Fig. 3.

magnitude was found to be independent of the input LER magnitude.

Figure 6 shows a direct comparison of the two LTF modeling methods presented above as well as the analytical LTF from the previous section. The analytical LTF is depicted by the solid curve, the white-noise calculated LTF is depicted by the diamond symbols, and the single-frequency-probe calculated LTF is depicted by the square symbols. It is evident that the various LTF calculation methods agree extremely well. The small differences between the

modeling methods and the analytical method can be attributed to the incorporation of the wavefront error in the modeling methods causing the modulation to drop slightly relative to the diffraction-limited case.

Having calculated the LTF for the engineering test stand Set-2 optic, it is now possible to predict the aerial-image-LER PSD contribution from the mask LER for any given mask. To this end, we calculate the real mask LER from a scanning electron microscope image of an actual EUV mask used in recent printing experiments.¹⁰ The plot in Fig. 7 shows the

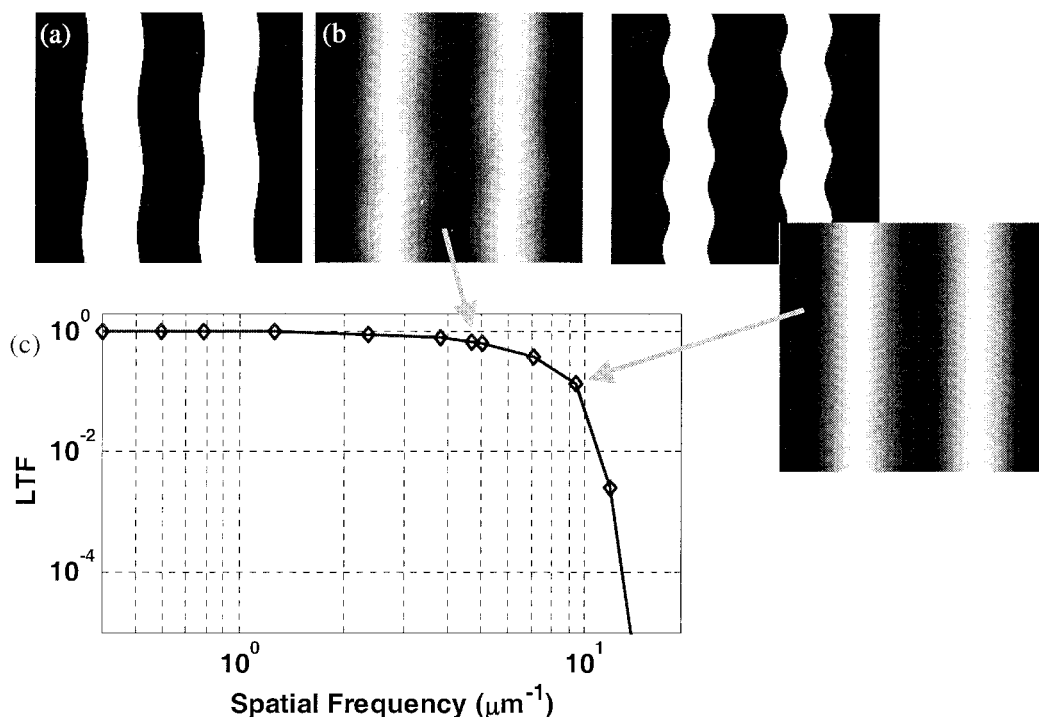


Fig. 5. LTF (a) shows an example probe mask, (b) its resulting aerial image, (c) generated by calculating the system response to a series of single-frequency LER probes.

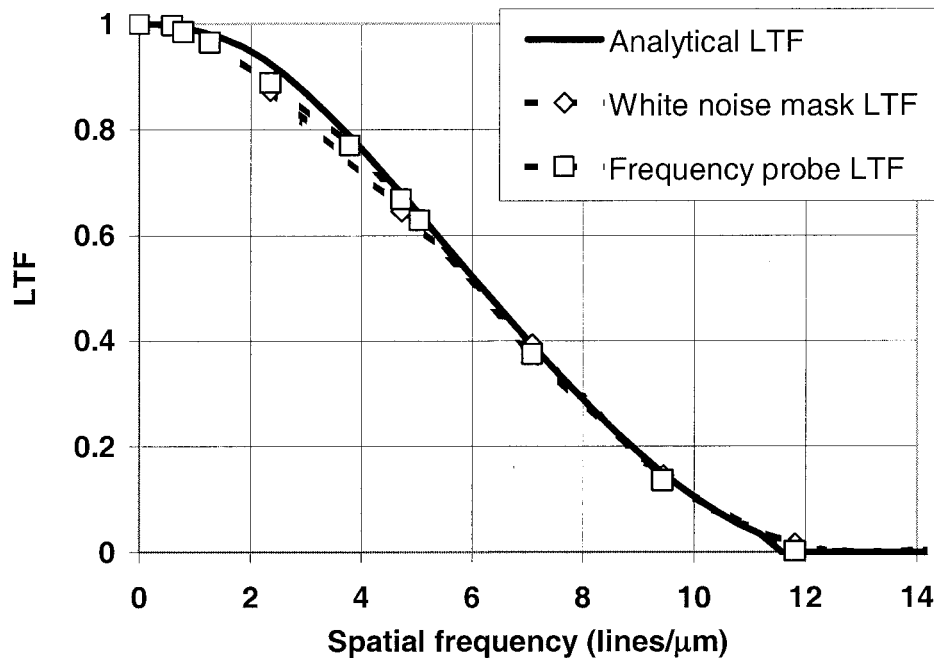


Fig. 6. Direct comparison of the two LTF modeling methods and the analytical LTF calculation. The analytical LTF is depicted by the solid curve, the white-noise calculated LTF by the open diamonds and the single-frequency-probe calculated LTF by the open squares. The small differences between the modeling methods and the analytical method can be attributed to the incorporation of the wavefront error in the modeling methods causing the modulation to drop slightly relative to the diffraction-limited case.

LER PSD measured from 100-nm coded features on the mask. We note that the peak at the 3-nm period is a scanning electron microscope artifact and contributes a negligible amount of energy to the LER, which in this case is 2.6 nm (a single-sided 3σ value) in image-plane coordinates (4 times reduction relative to the actual mask coordinates). To predict the mask contribution to the aerial-image- LER , we simply multiply the mask LER PSD by the square of the LTF. Figure 8 shows the resulting PSD (gray curve) along with resist-image LER PSDs for two different experimental EUV resists, both provided by the Ship-

ley Company. The 22 mJ/cm^2 sensitivity resist yielded an LER of approximately 3.6 nm, while the 2.0 mJ/cm^2 sensitivity resist yielded an LER of approximately 6.4 nm. In each case, the aerial-image- LER PSD is seen to be significantly lower than for the typical resist LER PSDs even at low spatial frequencies. Additionally, the sharp roll-off in the aerial-image- LER PSD at approximately 10 lines per μm is not replicated in the resist PSDs. Taking the mask contribution to the LER and assuming it to add in quadrature to other LER contributors, we see that even for the best LER case of 3.6 nm, the mask is only

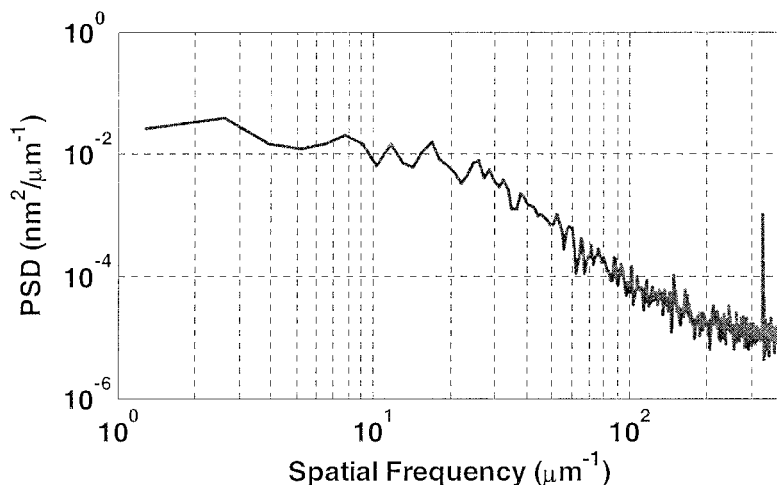


Fig. 7. LER PSD calculated from an EUV mask used in recent printing experiments. The LER PSD is measured from 100-nm coded features on the mask. The peak at the 3-nm period is a scanning electron microscope artifact and contributes a negligible amount of energy to the LER, which in this case is 2.6 nm in image-plane coordinates.

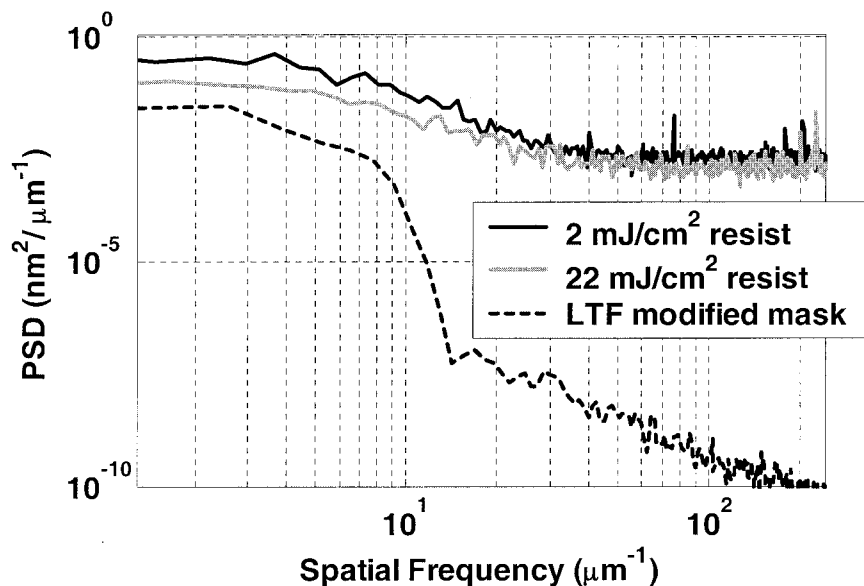


Fig. 8. Mask contribution to the aerial-image-LER (LTF modified mask), determined by multiplying the mask LER PSD by the square of the LTF along with resist-image LER PSDs for two different EUV resists. The 22 mJ/cm² sensitivity resist yielded an LER of approximately 3.6 nm, while the 2.0 mJ/cm² sensitivity resist yielded an LER of approximately 6.4 nm.

responsible for 0.2 nm (approximately 6%). These results demonstrate that, presently, mask technology is not a limiting factor in the LER characterization of EUV resist.

Finally, it is also interesting to directly compare the LTF to the MTF. Figure 9 shows the MTF (solid trace), the white-noise calculated LTF (open diamonds), and the single-frequency-probe calculated LTF (open squares). We note that what is referred to here as the MTF is actually the square wave transfer function under partially coherent illumination, where the illumination conditions are identical to those described above for the LTF modeling. It is evident that the LTF has a sharper roll-off than does the MTF. The faster roll-off is due to the two-dimensional nature of the LER and its interaction

with the point-spread function as compared with a pure one-dimensional line situation treated by the MTF. Also evident is that the LER coupling is stronger than predicted by the MTF at very low frequencies. This is due to the fact that the low end of the MTF reduction is dominated by flare [effectively a DC (uniform) background] that does not effect LER coupling; in the case of low-frequency structures effected by flare, the pattern will be faithfully reproduced with a simple DC offset, because the LER is quantified here assuming an ideal threshold resist model, flare has little effect on the LER. We note that this may not be the case in general for actual resist LER, in which case the reduced line-edge slope could increase the LER, yet this is a fundamentally different effect than the mask-LER coupling issue of concern here.

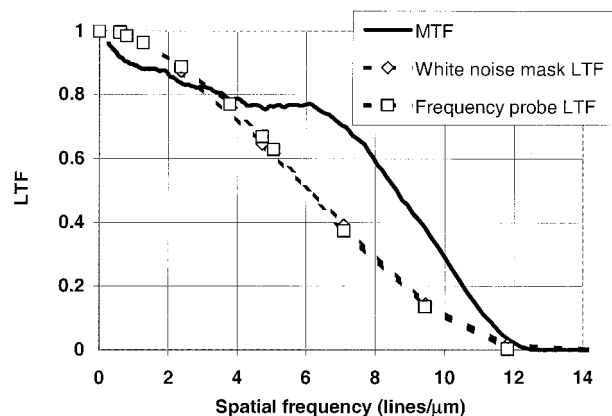


Fig. 9. Direct comparison of LTF and MTF. What is referred to here as the MTF is actually the square wave transfer function under partially coherent illumination, where the illumination conditions are identical to those described in Fig. 6 with respect to the LTF modeling.

4. Summary

The concept of the line-edge roughness transfer function (LTF) has been presented. This transfer function has been explicitly shown to differ fundamentally from the standard MTF and OTF. Using this concept we have shown current EUV resist characterization tests based on 0.1-NA projection optics to not be limited by mask LER issues. We note, however, that repeating the above analysis for an ideal 0.25-NA imaging optic and assuming the same mask LER as used above, the mask contribution to the aerial-image LER would be 1.8 nm. This mask contribution to the LER alone is almost equal to the full resist LER budget at the 50-nm node. Thus it is evident that future resist LER testing based on projection lithography will require improved masks.

This research was supported by the Extreme Ultraviolet Limited Liability Company and the Direc-

tor, Office of Science, Office of Basic Energy Science, of the U.S. Department of Energy under contract No. DE-AC03-76SF00098.

References

1. R. Stulen and D. Sweeney, "Extreme ultraviolet lithography," *IEEE J. Quantum Electron.* **35**, 694–699 (1999).
2. H. Meiling, J. Benschop, R. Hartman, P. Kürz, P. Høghøj, R. Geyl, and N. Harned, "EXSTATIC: ASML's α -tool development for EUVL," *Proc. SPIE* **4688**, 1–10 (2002).
3. K. Hamamoto, T. Watanabe, H. Hada, H. Komano, S. Kishimura, S. Okazaki, and H. Kinoshita, "Fine pattern replication on 10×10 -mm exposure area using the ETS-1 laboratory tool in HIT," *Proc. SPIE* **4688**, 664–671 (2002).
4. International Technology Roadmap for Semiconductors, 2001 Edition, (<http://public.itrs.net/>).
5. R. Brainard, C. Henderson, J. Cobb, V. Rao, J. Mackevich, U. Okoroanyanwu, S. Gunn, J. Chambers, and S. Connolly, "Comparison of the lithographic properties of positive resists upon exposure to deep- and extreme-ultraviolet radiation," *J. Vac. Sci. Technol. B* **17**, 3384–3389 (1999).
6. M. Shumway, S. Lee, C. Cho, P. Naulleau, K. Goldberg, and J. Bokor, "Extremely fine-pitch printing with a $10\times$ Schwarzschild optic at extreme ultraviolet wavelengths," *Proc. SPIE* **4343**, 357–362 (2001).
7. W. Li, H. Solak, and F. Cerrina, "EUV nanolithography: sub-50 nm L/S," *Proc. SPIE* **3997**, 794–798 (2000).
8. T. Watanabe, H. Kinoshita, A. Miyafuji, S. Irie, S. Shirayone, S. Mori, E. Yano, H. Hada, K. Ohmori, and H. Komano, "Lithographic performance and optimization of chemically amplified single-layer resists for EUV lithography," *Proc. SPIE* **3997**, 600–607 (2000).
9. J. Goldsmith, K. Berger, D. Bozman, G. Cardinale, D. Folk, C. Henderson, D. O'Connell, A. Ray-Chaudhuri, K. Stewart, D. Tichenor, H. Chapman, R. Gaughan, R. Hudyma, C. Montcalm, E. Spiller, J. Taylor, J. Williams, K. Goldberg, E. Gullikson, P. Naulleau, and J. Cobb, "Sub-100-nm lithographic imaging with the EUV $10\times$ Microstepper," *Proc. SPIE* **3676**, 264–271 (1999).
10. P. Naulleau, K. Goldberg, E. Anderson, D. Attwood, P. Batson, J. Bokor, P. Denham, E. Gullikson, B. Harteneck, B. Hoef, K. Jackson, D. Olynick, S. Rekawa, F. Salmassi, K. Blaedel, H. Chapman, L. Hale, P. Mirkarimi, R. Soufli, E. Spiller, D. Sweeney, J. Taylor, C. Walton, D. O'Connell, R. Stulen, D. Tichenor, C. Gwyn, P. Yan, and G. Zhang, "Sub-70-nm EUV Lithography at the Advanced Light Source Static Microfield Exposure Station Using the ETS Set-2 Optic," *J. Vac. Sci. & Technol. B*, **20**, 2829–2833 (2002).
11. J. W. Goodman, *Introduction to Fourier Optics*, 2nd ed. (McGraw-Hill, New York, 1996) Chap. 6, pp. 126–165.
12. D. Tichenor, A. Ray-Chaudhuri, S. Lee, H. Chapman, W. Replogle, K. Berger, R. Stulen, G. Kubiak, L. Klebanoff, J. Wronosky, D. O'Connell, A. Leung, K. Jefferson, W. Ballard, L. Hale, K. Blaedel, J. Taylor, J. Folta, E. Spiller, R. Soufli, G. Sommargren, D. Sweeney, P. Naulleau, K. Goldberg, E. Gullikson, J. Bokor, D. Attwood, U. Mikan, R. Hanzen, E. Panning, P. Yan, J. Bjorkholm, and C. Gwyn, "Initial results from the EUV engineering test stand," *Proc. SPIE* **4506**, 639–645 (2001).
13. D. W. Sweeney, R. Hudyma, H. N. Chapman, and D. Shafer, "EUV optical design for a 100 nm CD imaging system," *Proc. SPIE* **3331**, 2–10 (1998).
14. K. Goldberg, P. Naulleau, J. Bokor, and H. Chapman, "Testing EUV optics with visible-light and EUV interferometry," to be published, *J. Vac. Sci. & Technol. B*, **20**, 2834–2839 (2002).